Urchin-like Na-doped zinc oxide nanoneedles for low-concentration and exclusive VOC detections

Yiwen Zhou[1], Yifan Luo[1,2], Zichen Zheng[1], Kewei Liu[1,2], Xiaoxi He[1], Kaidi Wu[1], Marc Debliquy[2], Chao Zhang[1,✉]

[1] *College of Mechanical Engineering, Yangzhou University, Yangzhou 225127, China*
[2] *Material Science Department, University of Mons, Mons 7000, Belgium*

Abstract: In the early-stage diagnosis of lung cancer, the low-concentration (< 5 ppm) volatile organic compounds (VOCs) are extensively identified to be the biomarkers for breath analysis. Herein, the urchin-like sodium (Na)-doped zinc oxide (ZnO) nanoneedles were synthesized through a hydrothermal strategy with the addition of different contents of citric acid. The Na-doped ZnO gas sensor with a 3 : 1 molar ratio of Na^+ and citric acid showed outstanding sensing properties with an optimal selectivity to various VOCs (formaldehyde (HCOH), isopropanol, acetone, and ammonia) based on working temperature regulation. Specifically, significantly enhanced sensitivity (21.3@5 ppm) compared with pristine ZnO (~7-fold), low limit of detection (LOD) (298 ppb), robust humidity resistance, and long-term stability of formaldehyde sensing performances were obtained, which can be attributed to the formation of a higher concentration of oxygen vacancies (20.98%) and the active electron transitions. Furthermore, the improved sensing mechanism was demonstrated by the exquisite band structure and introduction of the additional acceptor level, which resulted in the narrowed bandgap of ZnO.

Keywords: zinc oxide (ZnO); heterovalent ions doping; citric acid; gas sensor; volatile organic compound (VOC) detection; lung cancer

1 Introduction

Lung cancer screening, particularly early-stage screening, has emerged as a topic of significant concern in the medical field for its positive effects on improving lung cancer survival rate [1–3]. Breath analysis, as a prospective technique for detecting lung cancer early, relies on detecting the concentration difference of specific volatile organic compounds (VOCs) presenting in the exhaled breath of both healthy individuals and patients, which possesses the advantages of non-invasive detection with rapid features and low cost, having so far shown promise as a diagnosis tool for early detection of lung cancer [4,5]. Many VOCs, including isopropanol [6], acetone [7], formaldehyde (HCHO) [8], and toluene [9], have been identified as lung cancer biomarkers due to their comparatively large concentration difference. However, most VOCs exist in exhaled breath usually at a very low concentration (< 1 ppm) [10]. Therefore, there is a challenge for monitoring different lung cancer biomarker VOCs at a ppb-level.

Since semiconductor metal oxide (MOX) sensors are mostly sensitive to VOCs and easy to obtain [11–13], they are prospective to exhibit a response even at a low concentration of lung cancer biomarker VOCs. Among diverse metal oxides, zinc oxide (ZnO) is usually employed as a gas-sensing material due to its wide bandgap, large exciton binding energy, great sensitivity to various types of VOCs, and ease of adjusting the morphology [14,15]. However, in the realm of VOC detection, pure metal oxides typically exhibit a detection concentration range in the order of tens to hundreds of ppm. Achieving the detection of ultra-low concentration VOCs necessitates the modification of metal oxides to enhance their responsiveness to low-concentration VOCs. It may be an impediment to the practical application of detecting lung cancer biomarkers, which needs to exhibit a high sensitivity even at ppb concentrations and provide different signals to various VOCs.

Doping ZnO with other metal or non-metal ions can introduce additional impurity levels within the bandgap of ZnO. These impurity levels typically occur near the top of the valence band (VB) or the bottom of the conduction band, allowing electrons at the impurity levels to absorb and transition with less energy. Simultaneously adjusting the surface adsorption state of oxygen can enhance performance [16–18]. Metal ion doping is effectively used to improve the sensing performance of ZnO. Specially, ZnO is highly sensitive to alkali metal elements and exhibits good doping stability, which will make it easier for ions to be doped into the lattice of ZnO, leading to the formation of more oxygen vacancies [19]. In addition, the solubility of alkali metals in the ZnO lattice is closely related to the radius of the dopant ions, and a low concentration of doping will make it difficult to generate the acceptor energy level. Na ions have a higher radius than Zn ions and show high solubility [20]. It is favorable to improve the stable concentration of Na doping, leading to the formation of the shallow acceptor level [21,22]. Therefore, Na ion doping has a significant advantage in adjusting the surface state and band structure of ZnO to optimize the gas-sensitive properties. The Na-doped ZnO nanoflowers were fabricated by Jaisutti *et al.* [20] via simple chemical precipitation. Their ability to detect acetone at ppm-levels was subsequently examined with ultraviolet (UV) light irradiation. The response to 1 ppm acetone was 52% with

✉ Corresponding author.
E-mail: zhangc@yzu.edu.cn

5 mW·cm^{-2} UV light. Mariappan *et al.* [23] fabricated a Na-doped ZnO sensor by nebulizer spray pyrolysis method which showed a needle-like structure and the coating was porous. The sensor was sensitive to 50 ppm ammonia ($S = 0.6$) at 200 ℃. Basyooni *et al.* [24] prepared Na-doped ZnO by sol–gel method, and the sensor showed an extremely high response (80%) to CO_2 in nitrogen, which is almost 80 times higher compared with the undoped ZnO. Additionally, nanostructures with elevated specific surface areas, particularly those possessing multidimensional configurations, are advantageous for enhancing gas sensing sites and improving gas sensitivity performance [25,26]. However, most research has shown limited improvement in the sensing performance of ZnO. Especially, a higher response at a low concentration requires a further breakthrough. In addition, research focusing on the detection of formaldehyde and isopropanol is still limited.

Herein, the urchin-like Na-doped ZnO nanoneedles were synthesized with the assistance of citric acid via the hydrothermal method. The doping amount of citric acid plays an important role in the doping of Na$^+$. The sensing properties of Na-doped ZnO sensors were greatly improved compared with pristine ZnO, displaying a high response (~21.3) towards low concentration biomarkers (5 ppm) at 50% relative humidity (RH), along with a low limit of detection (LOD) (298 ppb), humidity resistance, and stability, which is beneficial to the practical breath analysis. The surface chemical state and the band structure were analyzed according to the X-ray photoelectron spectroscopy (XPS) and VB-XPS to investigate the enhanced gas-sensing mechanism.

2 Experimental

2.1 Synthesis of ZnO and Na-doped ZnO nanoneedles

All reagents (VWR, Belgium) were used without further purification. To synthesize the Na-doped ZnO, NaF was used as the Na$^+$ source, and citric acid as the ligand. The following is the specific synthesis procedure: 3 mmol $Zn(NO_3)_2$·6H$_2$O and 0.15 mmol NaF were dissolved in 44 mL deionized (DI) water. After magnetically stirring for 15 min, 0.05 mmol of citric acid was added into the beaker and stirred for an additional 15 min to form solution A. At the same time, solution B was formed by dissolving 1 g of cetyl trimethyl ammonium bromide (CTAB) in 22 mL absolute ethanol and magnetically stirring until the powders were dissolved completely. The resulting solution A and solution B were then mixed and stirred for 15 min. Then 30 mmol

85% KOH tablets were added into the mixture and stirred until all the pills were dissolved to form solution C. Subsequently, 1 mL of ethylenediamine mixed with 9 mL of DI water was added into solution C and kept stirring until the final solution reached a uniform consistency, resulting in the formation of the precursor. Finally, the precursor was placed into a 100 mL teflon-lined autoclave and then reacted at 100 ℃ for 2 h. The resulting sediments were repeatedly rinsed with DI water and absolute ethanol until the pH of the supernatant reached 7. The obtained white sediments were dried at 80 ℃ overnight. The pure ZnO nanoneedles were synthesized using the same methods without citric acid and NaF. To study the effect of Na$^+$ and citric acid, the samples with only NaF addition and 0.025, 0.05, and 0.1 mmol citric acid addition Na-doped ZnO (the proportion of NaF and citric acid were 6 : 1, 3 : 1, and 3 : 2, respectively) were named as NaZnO, NaZnO0.5, NaZnO1, and NaZnO2. Figure 1 exhibits the brief synthesis route of Na-doped ZnO powders.

2.2 Materials

X-ray diffraction (XRD) tests were conducted using a Bruker D5000 instrument to analyze the phase and crystallinity of all powder samples coated on Al$_2$O$_3$ substrates. The measurements were performed with Co Kα1 radiation ($\lambda = 1.789$ Å) ranging from 20° to 80° at 5 (°)·min^{-1}, and a slow scan was carried out next to the main peak of ZnO at 0.5 (°)·min^{-1} to further check the peak shift of Na-doped ZnO. The morphologies of all powder samples and the ZnO and NaZnO1 sensors were examined using a field emission-scanning electron microscope (FE-SEM; SU8020, Hitachi, Japan). A high-resolution transmission electron microscope (HRTEM; Tecnai G2 F30, FEI, USA) was used to examine the structure of the ZnO powders. All powder samples were dissolved in anhydrous ethanol and dispersed ultrasonically. XPS and VB-XPS were utilized to assess the elemental composition. The analysis was performed using an X-ray photoelectron spectroscope (Phi Versa Probe 5000, Ulvac-Phi, Japan). The XPS analysis chamber maintained a pressure of approximately 1.10×10^{-9} Torr. The utilized X-ray source was monochromatized, using the Al Kα line ($E = 1486.7$ eV). The X-ray source was powered at 50 W while the beam voltage used was 15,000 V. To prove the Na amount added to the sample is correct, we did an inductively coupled plasma optical emission spectroscopy (ICP-OES) measurement. For ICP-OES measurement, all Na-doped ZnO powder samples were dissolved in 5% nitric acid (HNO$_3$), the concentration of which was fixed at
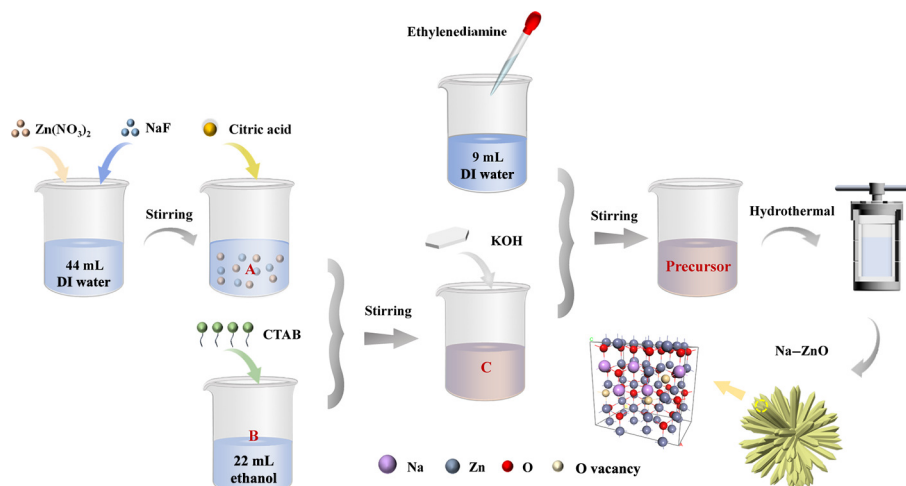

Fig. 1 Synthesis route of Na-doped ZnO samples.

10 ppm, as the target samples to be tested. Moreover, reference samples were prepared by mixing 0 ppm, 2 ppm, 4 ppm, 6 ppm, 8 ppm, and 10 ppm NaF and $Zn(NO_3)_2$ in 5% HNO_3. Ultraviolet–visible (UV–Vis) spectra were carried out via ultraviolet–visible-near infrared (UV–Vis-NIR) spectrophotometer (Cary 5000, Varian, USA). The Brunauer–Emmett–Teller (BET) method was carried out by Autosorb IQ3 (Quantachrome Instruments, USA) to analyze the BET surface area according to the isotherms of nitrogen adsorption/desorption. More information about the sample preparation can be found in Section S1 in the Electronic Supplementary Material (ESM).

2.3 Gas sensing setup

The sensor used in our study consisted of Al_2O_3 substrate (5 cm in length and 1 cm in width) with Au interdigital electrodes (with an electrode spacing of 250 μm) and Pt heating wires on both sides (Fig. S1 in the ESM). The gas sensors were made using the drop-casting method: A mixture of 50 mg as-prepared powders and 0.5 mL deionized water was prepared, and then a homogeneous slurry was obtained by grinding with a mortar and pestle. Next, the obtained slurry was added dropwise onto the conductive electrode portion of the sensor using a pipette gun, as shown in Fig. S2 in the ESM. The ZnO and the Na-doped ZnO sensors were obtained after being dried at 100 ℃ in an oven for over 16 h. The sensors were pre-heated for more than 72 h to eliminate potential organic impurities and surface contamination before the test. The sensor measurement was carried out with a homemade apparatus, as shown in Fig. S1 in the ESM. More testing details can be found in Section S2 in the ESM.

In the gas sensing test, the response (S) is defined as $(R_a - R_g)/R_g$, where the resistance in synthetic air is represented by R_a, while the resistance in the target gas is denoted by R_g. The response/recovery time were defined as the duration required to achieve a 90% change in resistance during the complete sensing cycle.

3 Results and discussion

3.1 Material characterization

The crystal structure of Na-doped ZnO was investigated using XRD. Figure 2(a) depicts the peaks for ZnO, NaZnO, NaZnO0.5, NaZnO1, and NaZnO2. The diffraction peaks observed in all samples correspond to the hexagonal structure of ZnO (PDF#No.99-0111), which is the same as the pure ZnO we measured before. All the peaks are strong and narrow, with no other characteristic peaks found in any of the samples, which indicates the excellent crystallinity and high purity of ZnO. Since the powder quantity and uniformity could be different on various test substrates (Al_2O_3), there were certain differences in the intensity of the peaks of Al_2O_3.

The crystal structure of ZnO did not change with the doping of Na ions. For further analysis, a slow scan was tested around the main peak of ZnO ranging from 41° to 45°, which is related to (101) facet. Figure 2(b) illustrates a noticeable shift towards a lower angle range following the doping of Na, which means the increase of the interplanar spacing value according to Bragg's law (Eq. (1)). Since the diameter of Na^+ ions (1.02 Å) is larger than that of Zn^{2+} (0.74 Å) ions [27,28], it is possible that the Na^+ substitutes the Zn^{2+} in the ZnO lattice.

$$2d\sin\theta = n\lambda \tag{1}$$

$$D = k\lambda/(\beta\cos\gamma) \tag{2}$$

where d represents the interplanar spacing value (Å); θ stands for the diffraction angle; n represents the diffraction order; λ denotes the wavelength of Co Kα1 radiation ($\lambda = 1.789$ Å), which serves as the X-ray source; k represents the shape factor ($k = 0.89$); β represents the full width at half maximum (FWHM); and γ represents the position of the main peak of ZnO corresponding to the (101) facet. Scherrer equation (Eq. (2)) was used to calculate the average grain size of ZnO and Na-doped ZnO. The crystallite size of ZnO, NaZnO, NaZnO0.5, NaZnO1, and NaZnO2 calculated by the Scherrer equation (Eq. (2)) are 55.0, 37.9, 39.6, 36.1, and 37.8 nm, respectively. More calculated data were described in Table S1 in the ESM. As illustrated in Fig. 2(c), with the doping of Na^+, the average grain size shows an obvious decrease. This indicates that Na ions were referred to as the nucleation centers, leading to the production of the crystals [29]. The smaller grain size is advantageous for improving gas sensitivity performance [30].
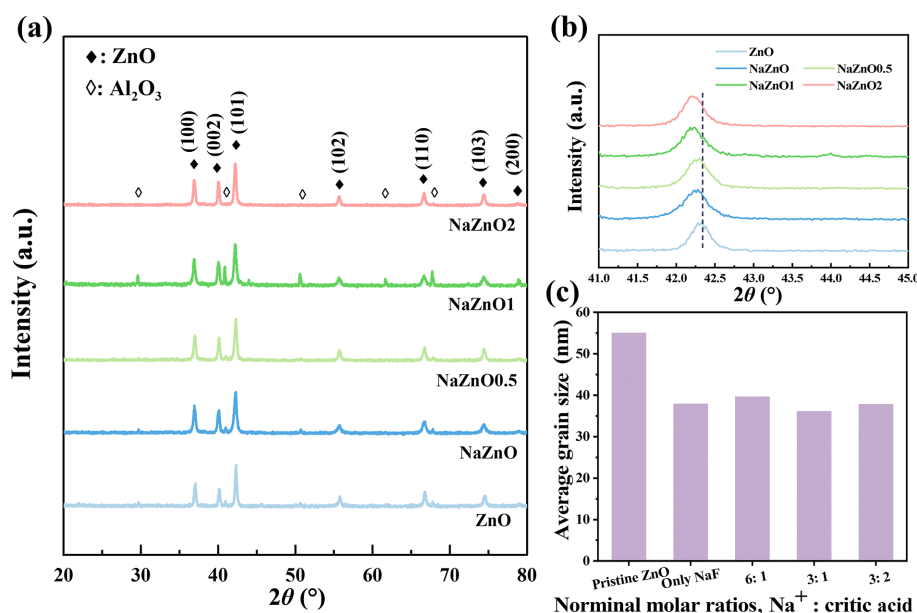

Fig. 2 (a) XRD patterns of ZnO and Na-doped ZnO samples coated on alumina substrates. (b) Slow scanning close to the main peak of ZnO, and (c) average grain size of all samples.

The microstructure and morphology of all samples were observed via FE-SEM and TEM tests. Both the pristine ZnO and the Na-doped ZnO samples show a similar urchin-like structure assembled by nanoneedles (Figs. 3(a)–3(e)). The length of each nanoneedle is around 3 μm, while the diameter is about 100 nm. The low-magnification FE-SEM images of ZnO and Na-doped ZnO samples can be found in Section S3 in the ESM, as shown in Fig. S4 in the ESM. The morphology of these samples does not significantly change, which indicates that neither the doping of Na nor the addition of citric acid has a big influence on the morphology. Figures 3(f) and 3(g) depict the structure of pure ZnO and Na-doped ZnO with citric acid after being coated on the sensor substrate. The urchin-like morphology of the two sensors remains similar.

However, the only difference is that the surface of ZnO sensing layers has a porous structure, attributed to the evaporation of water from the slurry during the preparation of the sensing layer, creating a porous surface for the ZnO sensing layers. This porous structure has the potential to enhance the specific surface area of the sensing layer, thereby improving the gas sensing performance. From the TEM images of NaZnO presented in Figs. 3(h) and 3(i), it is evident that the nanoneedles comprised many nanoparticles. The HRTEM image of the NaZnO powders is shown in Fig. 3(j).

It can be analyzed that the interplanar spacing of 0.264 nm corresponds to the (002) plane of hexagonal ZnO. Compared with the pure ZnO (d = 0.260 nm), the increased interplanar space is attributed to the doping of Na. Since the diameter of Na^+ is larger than Zn^{2+}, Na ions reside in the interstitial or substitutional Zn sites. To check the amount of Na^+ doped in the ZnO lattice, energy-dispersive spectrometry (EDS) and ICP-OES tests were carried out. Due to the similar position of Na and Zn peaks in EDS shown in Fig. S5 in Section S3 in the ESM, it is impossible to confirm the amount of Na by EDS, so the concentration of Na^+ was determined using the ICP-OES method. Figures 3(k)–3(m) depict the EDS mapping of NaZnO1. It confirms the uniform distribution of the Na, Zn, and O elements. The ICP-OES results of the atom ratio of Na in NaZnO, NaZnO0.5, NaZnO1, and NaZnO2 samples are 2.62%, 6.02%, 7.42%, and 6.56%, respectively. It can be found that with citric acid, the Na concentration is similar to the value we added into the solution, but without the assistance of citric acid, only about half of Na is successfully doped, demonstrating that citric acid has a crucial role in the Na doping of ZnO crystal.
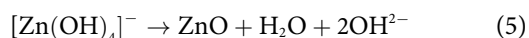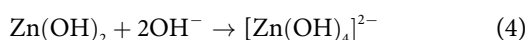
The synthesis mechanism of Na-doped ZnO nanoneedles is based on the Ostwald ripening mechanism. When KOH flakes are added to the solution, the dissolved OH^- ions react with the Zn^{2+}
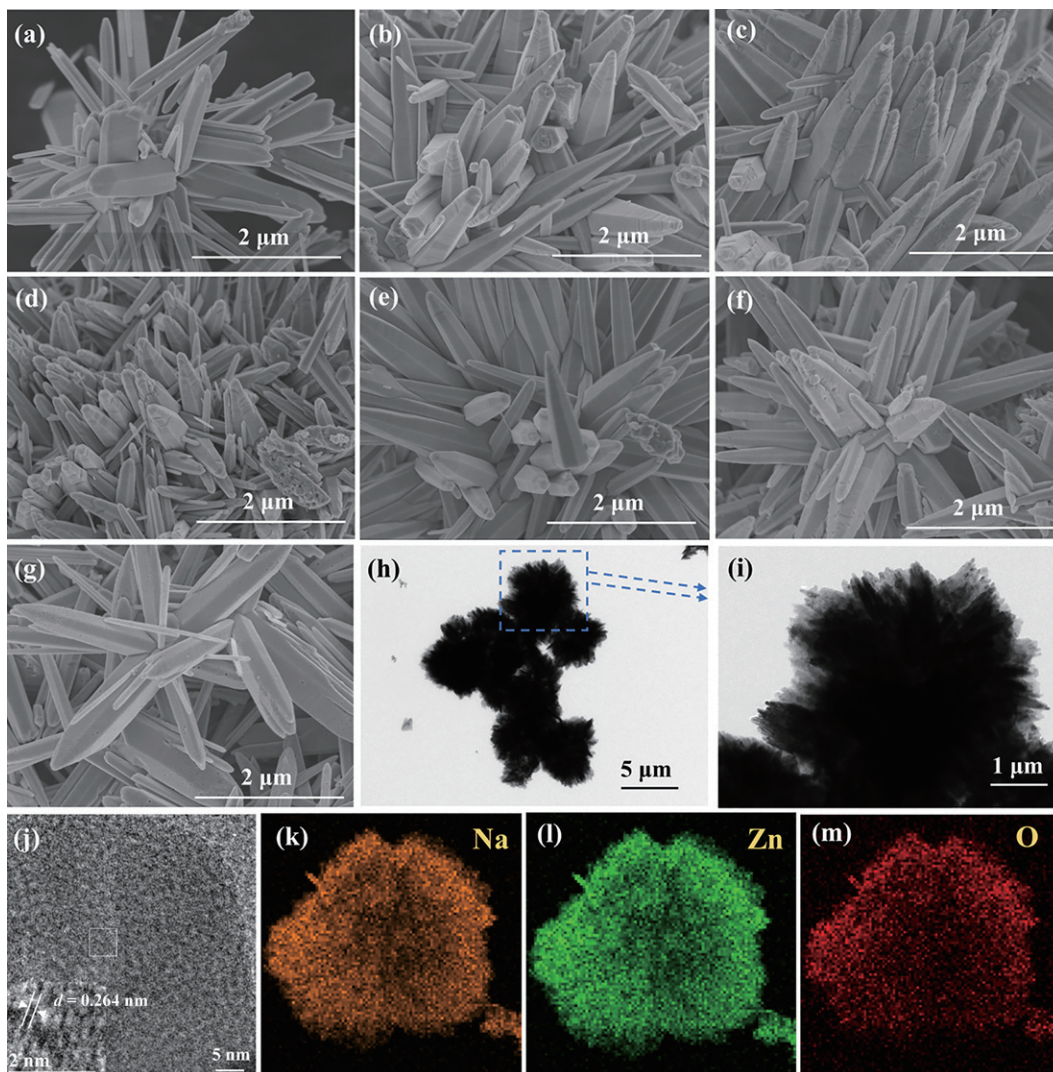
Fig. 3 SEM images of (a) ZnO powders, (b) NaZnO0.5 powders, (c) NaZnO powders, (d) NaZnO1 powders, (e) NaZnO2 powders, (f) ZnO sensing layer, and (g) NaZnO1 sensing layer. (h–j) TEM images of NaZnO1 powder. (k–m) EDS mappings of Na, Zn, and O elements.

ions formed by the dissolution of $Zn(NO_3)$, resulting in flocculent $Zn(OH)_2$ precipitates (Reaction (3)). With the further dissolution of NaOH, the concentration of OH^- in the solution increases, leading to the disappearance of the white flocculent precipitate (in this work, the amount of added OH^- is ten times that of Zn^{2+}, and the excess OH^- continues to combine with $Zn(OH)_2$ creating $[Zn(OH)_4]^{2-}$ (Reaction (4)).

When this solution reacts under high temperature and pressure conditions in a reaction vessel, $[Zn(OH)_4]^{2-}$ hydrolyzes to form crystalline ZnO (Reaction (5)). CTAB plays a templating role in the synthesis process. CTAB, as a surfactant, has a second critical micelle concentration in water of 2.1×10^{-2} mol·L^{-1}. Above this concentration, CTAB micelles self-assemble into rod-like structures, while below this concentration, they form spherical structures. In the above structure, the positively charged end of CTAB is oriented outwards, exhibiting higher surface energy and easily binding with the negatively charged $[Zn(OH)_4]^{2-}$. The $[Zn(OH)_4]^{2-}$ ions are encapsulated on the CTAB surface, leading to the crystallization of ZnO primarily taking place on the surface of CTAB micelles. This process ultimately leads to the formation of various nanostructures. Ethylenediamine acts as a complexing agent in the synthesis process, connecting $[Zn(OH)_4]^{2-}$.

$$Zn^{2+} + 2OH^- \rightarrow Zn(OH)_2 \qquad (3)$$

$$Zn(OH)_2 + 2OH^- \rightarrow [Zn(OH)_4]^{2-} \qquad (4)$$

$$[Zn(OH)_4]^- \rightarrow ZnO + H_2O + 2OH^{2-} \qquad (5)$$

To further investigate the information about the Na-doped ZnO sensors, the BET test was carried out (Fig. 4(a)). The specific surface area of NaZnO1 was 11.347 m^2·g^{-1}. The UV–Vis spectra of all samples illustrate an adsorption edge ranging from 399.87 to 408.83 nm, as shown in the inset of Fig. 4(b). As shown in Fig. 4(b), the bandgap energies (E_g) of all samples were calculated according to the Tauc plot (Eq. (6)).

$$Ah\nu = B(h\nu - E_g)^{1/n} \qquad (6)$$

where A is the absorbance, and B is a constant. Since the ZnO is a direct bandgap semiconductor, the value of n is 1/2 [31]. The calculated bandgaps of the ZnO and NaZnO1 samples were 3.19 and 3.15 eV, respectively. The separate plots for the calculated band gap energies for each sample (Figs. S6 and S7 in the ESM) can be found in Section S3 in the ESM. The narrowed bandgap will make it easier for electrons to transit.

To check the concentration of oxygen vacancies, we performed an XPS test on ZnO, NaZnO, and NaZnO1 samples. In Fig. 5(a),

the surveys of the three different samples were displayed. From the XPS survey, only peaks related to Zn, O, and C can be found, with no peaks related to Na$^+$ detected. Figures 5(b)–5(d) present the plotted and deconvoluted O 1s region of the three samples using a mixed function comprising 30% Lorentzian and 70% Gaussian components. The peaks at 530.2, 531.8, and 533.4 eV represent the existence of lattice oxygen (O_L), oxygen vacancy (O_V), and chemisorbed oxygen species (O_C) [32]. The concentration of oxygen vacancies was calculated as the ratio of the area of the O_V peak in regions (Figs. 5(b)–5(d)) to the total fitted peak area. The concentration of oxygen vacancies of ZnO, NaZnO, and NaZnO1 are 2.50%, 19.08%, and 20.98%, respectively. It indicates that Na doping induces the formation of more oxygen vacancies and free electrons. As the Na doping concentration increases, the content of oxygen vacancies also gradually increases, as analyzed by ICP-OES in Section 3.1. This will increase the number of available adsorption sites for gas molecules and enhance the donor electron ability of Na-doped ZnO, thereby improving the gas sensing performance.

3.2 Gas sensing performance

The working temperature for different VOC biomarkers of lung cancer was investigated at 50% RH syntenic air to better simulate the actual breathing environment. According to our experience before with ZnO, we chose the temperature range between 200 and 325 ℃ with four different families of gases (isopropanol, acetone, formaldehyde, and ammonia) which have the potential to serve as biomarkers to detect lung cancer and were representative with a higher concentration [33]. Figures 6(a)–6(d) depict the response change to 5 ppm isopropanol, acetone, formaldehyde, and 50 ppm NH$_3$ (the responses at 5 ppm were too small to abandon) with the change of working temperature. We conducted three replicates of the experiment, and the specific experimental data, along with their maximum deviation, can be found in Tables S2–S5 in the ESM. The operation temperatures range from 200 to 300 ℃. However, the maximum value was not observed for isopropanol, so a point at 325 ℃ was added as well. In general, the NaZnO1 sensor showed the best response among the five different sensors to all the target gases in this test. Another interesting behavior is the change of optimal working temperature with the doping of Na$^+$ to target gases. For all these sensors, the optimal working temperatures for isopropanol, acetone, and ammonia were similar, which is at 300 ℃ for isopropanol, 275 ℃ for acetone, and 250 ℃ for ammonia. However, the optimal temperature for formaldehyde is quite different. According to the curve, the sensors could be divided into two groups. For ZnO, NaZnO, and NaZnO0.5, these three sensors showed a similar trend. Their optimal temperature for HCHO is between 275 to

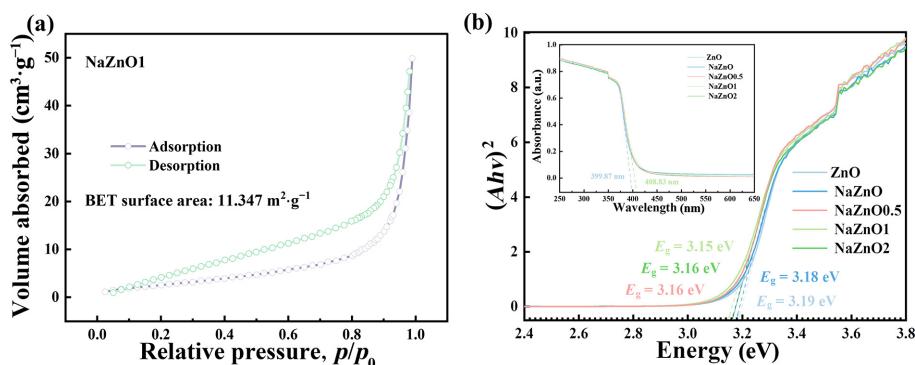**Fig. 4** (a) N$_2$ adsorption and desorption isotherms of NaZnO1. (b) Tauc plots of all samples (the inset shows the UV–Vis absorption spectra).
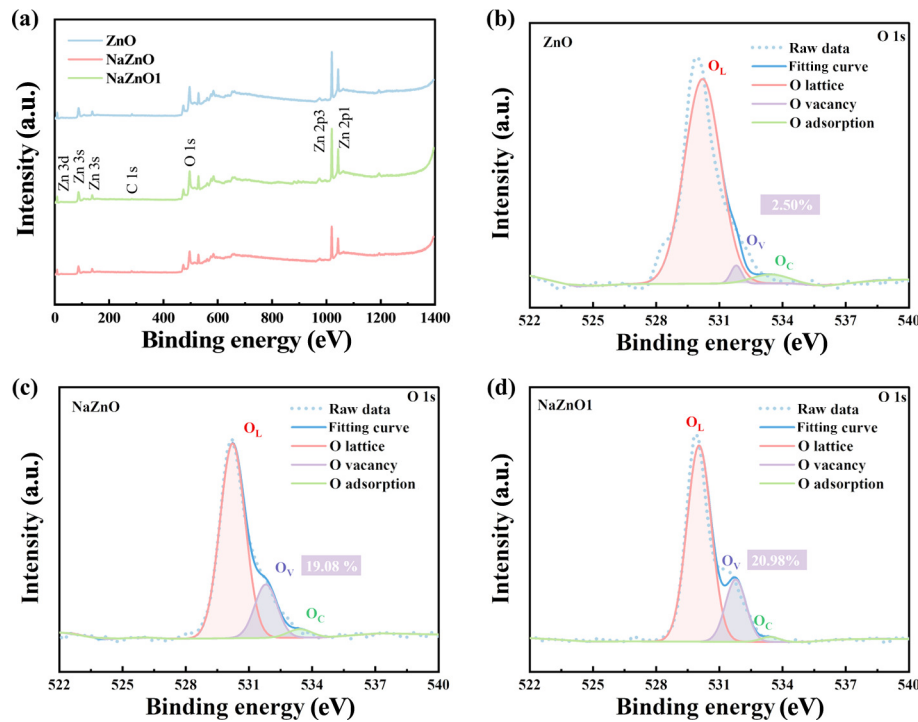
Fig. 5 (a) XPS survey of ZnO, NaZnO, and NaZnO1. (b) O 1s region of ZnO, (c) O 1s region of NaZnO, and (d) O 1s region of NaZnO1.
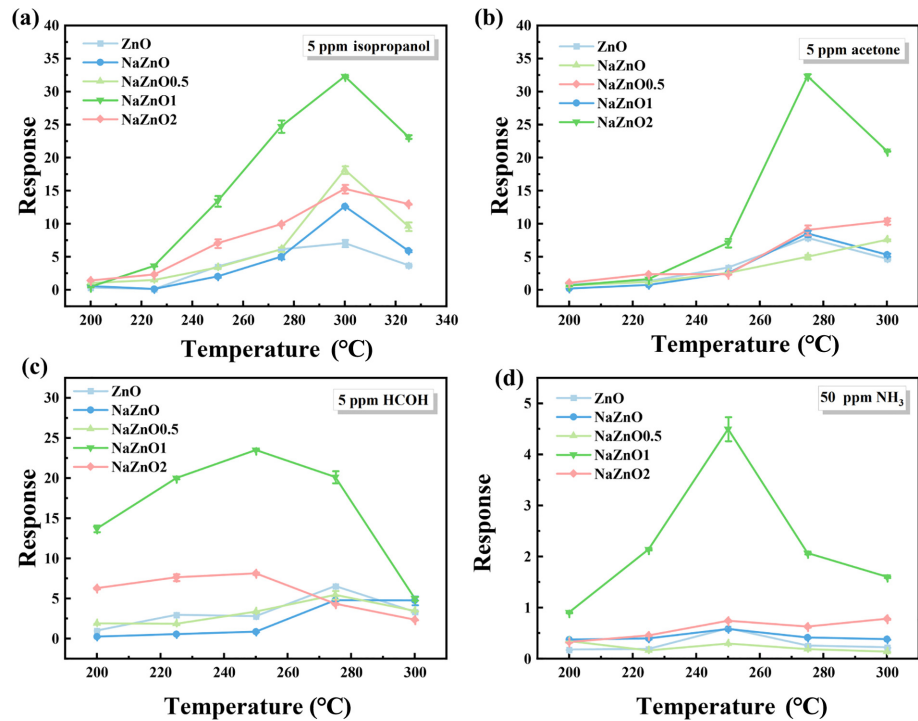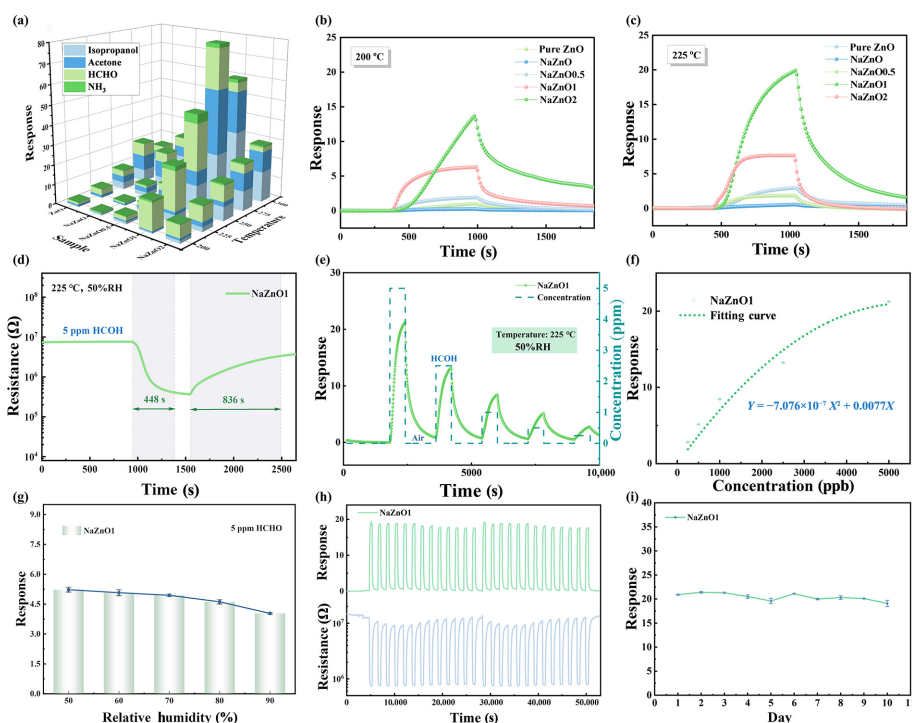

Fig. 6 Response change of all sensors to (a) 5 ppm isopropanol, (b) 5 ppm acetone, (c) 5 ppm HCOH, and (d) 50 ppm NH$_3$ with the change of working temperature with 50% RH (the error bars represent the maximum deviation from the average response of the three repetition tests).

300 ℃. When the temperature is lower than 275 ℃, their response had a significant drop. For NaZnO1 and NaZnO2, these two had the best response at 250 ℃. As the temperature increased, the response decreased quickly. When the temperature decreased from 250 ℃, a slight decrease in the response can also be found, but it was much slower than at the higher temperature range.

As shown in Fig. 7(a), the NaZnO1 sensor exhibited various selectivity to different VOCs with the change of working temperature. It was evident that at lower temperatures (200–250 ℃), the sensor exhibited a heightened responsiveness to

HCHO compared with other VOCs. Upon reaching 275 ℃, the acetone registered the highest response. Furthermore, as the temperature ascended to 300 ℃, the NaZnO1 sensor displayed a discerning and selective response to isopropanol. This phenomenon was intricately linked to the varying adsorption capacities of gas molecules on the sensing material surface at different temperatures and the degree of oxidation-reduction reactions. A detailed explanation can be found in Section 3.3. Table S6 in the ESM shows specific response values in Fig. 7(a). To further compare the selectivity of the NaZnO1 sensor at

Fig. 7 (a) Selectivity of all sensors at different working temperatures with 50% RH. Dynamic change of all sensors to HCHO at (b) 200 ℃ and (c) 225 ℃. (d) Response/recovery time of the NaZnO1 sensor to 5 ppm HCHO at 225 ℃, 50% RH. (e) Dynamic response of NaZnO1 sensor to HCHO at 200 and 225 ℃. (f) Mathematic fitting curve of the response of the NaZnO1 sensor to HCHO from 5 ppm to 0.25 ppm. (g) Response of the NaZnO1 sensor to 5 ppm HCHO at 225 ℃ with different relative humidities from 50% to 90% (error bars represent the maximum deviation from the average response of the three repetition tests). (h) Electrical resistance change and response change of the NaZnO1 sensor in a continuous cycling test with 26 cycles. (i) Stability test of NaZnO1 sensor with 5 ppm HCHO at 225 ℃ in 10 days (error bars represent the maximum deviation from the average response of three repetition tests).

different temperatures, we defined the ratio of the response to the target gas (S_{target}) to the response to interfering gases ($S_{interference}$) as K (the responses to 50 ppm NH_3 were negligible at all temperatures and were thus disregarded in quantitative comparisons). Calculation results (Table S7 in the ESM) revealed that the K values of HCHO at 200 and 225 ℃ were 29.7, 21.0 and 6.6, 13.2 for isopropanol and acetone, respectively. Since the K values of HCHO at 250 ℃ were relatively low, further research at 250 ℃ was not continued in the following experiments. Despite the higher responses to acetone and isopropanol at 275 and 300 ℃, there was poor selectivity (1.3, 1.6 for isopropanol and HCHO and 1.5, 6.5 for acetone and HCHO). Additionally, considering power consumption and practical application scenarios, we opted for HCHO, which exhibited high selectivity responses in the lower temperature range for further research.

To further investigate the sensors, Figs. 7(b) and 7(c) illustrate the response changes of the five sensors to HCHO at temperatures of 225 and 200 ℃, respectively. Although the selectivity at 200 ℃ is better than 225 ℃, the sensor had a very bad response and recovery rate at 200 ℃, as shown in Fig. 7(b). During the responding period, which was set as 10 min, the response at 200 ℃ was always increasing. For the recovery period, the resistance could only return to about 126% of the original baseline value before the injection of target gas in 20 min of recovery. The response/recovery rate may not be suitable for a portable device that would be used by a doctor for breath analysis. Considering the selectivity, response, and response/recovery rate, the optimal working temperature for the NaZnO1 sensor to detect HCHO should be 225 ℃. Figure 7(d) illustrates the response curve of the NaZnO1 sensor, which indicated a response/recovery time of 448 s/836 s.

Moreover, the dynamic electrical resistances of all samples were

illustrated in Fig. S8 in the ESM. It can be observed that the electrical resistance consistently decreased when in the target gases. This means that the Na-doped ZnO sensors were still n-type semiconductors. Furthermore, with the doping of Na^+, the resistance of the Na-doped ZnO sensors increased. This can be attributed to the increased thickness of the depletion layer for the Na^+ substituting some of the Zn^{2+} centers, leading to a decrease in charge carriers. Thus, the increased thickness of the intergranular potential barrier enhanced the difficulty of electron movement.

Figure 7(e) plots the dynamic and concentration–response curve of the NaZnO1 sensor tested at 225 ℃ and 50% RH. The average response values of NaZnO1 to 5000 ppb, 2500 ppb, 1000 ppb, 500 ppb, and 250 ppb in three repetition tests were 21.30, 13.24, 8.43, 5.14, and 2.80, respectively. The maximum deviations were 0.074, 0.047, 0.055, 0.045, and 0.017, which can prove that this sensor has a high and stable response to low concentrations of HCHO. As the concentration of formaldehyde increased, the response gradually increased, which is related to the larger quantity of gas and its more volatile nature. The numerical fitting result is depicted in Fig. 6(f). The response to HCHO in the low concentration range can be expressed by Eq. (7):

$$S = -7.076 \times 10^{-7} x^2 + 0.0077x \qquad (7)$$

LOD should be probed since the concentrations of lung cancer biomarker VOCs are usually as low as ppb-level. The LOD of the NaZnO1 gas sensor was calculated according to the the sensor noise (σ) and the slope ($M = 3.67$) of the fitting curve of the linear relationship between the response and the concentration of gas (Fig. S9 in the ESM). The calculated LOD was 0.298 ppm, which is equivalent to 298 ppb. It revealed a potential to employ in the breath analysis. More calculation details were provided in Section S4 in the ESM.

Table 1 compares the gas sensing performance of the Na-doped ZnO sensor fabricated in this work with some other alkali metal-doped ZnO sensors in the literature. Until now, few studies on alkali metal-doped ZnO sensors have been reported. Meanwhile, the types of semiconductors after alkali metal ion doping are different. In some cases, ZnO can be transformed into p-type semiconductors through alkali metal doping, while some materials are p-type according to the Hall effect test, but their gas sensing performance is consistent with n-type semiconductors. The Na-doped ZnO sensor prepared in this paper exhibits comparable or higher response even at significantly lower concentrations of lung cancer biomarkers than those reported in the literature, proving that the preparation method in this work can significantly improve the response performance of the Na-doped ZnO sensor to VOCs. In addition, according to the literature, alkali metal-doped ZnO sensors rarely use HCHO as the main target gas, while the NaZnO1 sensor in this study exhibits excellent gas sensing performance against HCHO at 225 ℃.
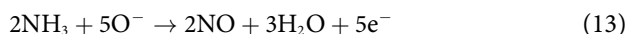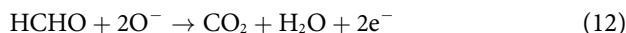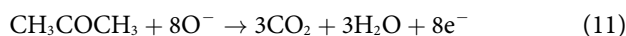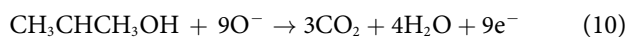
As mentioned before, for breath analysis, humidity is an important interference to the sensors especially when the working temperature is low. In Fig. 7(g), the relationship between RH and response to 500 ppb HCHO from 50% to 90% calculated at the working temperature of 225 ℃ was plotted. The response diminished as RH increased, which is consistent with the competitive adsorption of water molecules [34]. The response value dropped from 5.1 to 4 (the maximum deviation was 0.12, 0.15, 0.06, 0.11, 0.04, respectively) which is around 20%. This means this sensor is relatively stable to humidity change. Since the alcohol gases, including methanol and ethanol, can also serve as potential markers for lung cancer breath detection or as interference gases, we also conducted the selectivity of more interference gases (Fig. S10 in the ESM). The test results indicated that the sensor maintained a high selectivity for formaldehyde and exhibited relatively poor resolution for alcohol gases. Nevertheless, gas sensors used for respiratory monitoring in electronic noses do not necessarily require absolute selectivity but rather the ability to exhibit different signals for various gas types. To further validate the practicality of the sensor, we used the mixture of O_2 and 5 ppm of acetone, isopropanol, ethanol, methanol, and 50 ppm of NH_3 as carrier gases to detect the response of the NaZnO1 sensor to 5 ppm of HCHO (Fig. S11 in the ESM). The results revealed that under the background of the interfering gas, the NaZnO1 sensor still exhibited a high response (~16 to ~18.8@5 ppm HCHO), reaffirming its selectivity for HCHO.

Long-term stability is another crucial parameter for a gas sensor. The gas sensing performance of the NaZnO1 sensor at 225 ℃ to 5 ppm HCHO gas with 50% RH was tested for 26 cycles continuously. The resistance response changes with different cycles are plotted in Fig. 7(h). During the testing period, the average response of the 26 cycles was 19.30, while the standard deviation was 0.57. Based on the data, we can conclude that the NaZnO1 sensor exhibited good stability. Figure 7(i) shows the response test results of the NaZnO1 sensor under conditions of 275 ℃ and 50% relative humidity over a period of 10 days with three repetitive tests for each day (the maximum deviation can be found in Table S8 in the ESM). The sensor exhibited a consistently stable response throughout the testing period, with an average response value of 20.43 and a standard deviation of 0.717, signifying good stability.

3.3 Sensing mechanism

Figure 8(a) depicts the gas-sensing mechanism of Na-doped ZnO. First, O_2 molecules adsorbed the Na-doped ZnO surface. These adsorbed oxygen molecules then generated oxygen ions. O_2 exhibits varying forms of adsorption on the material surface at different temperatures [37,38]. Under the testing conditions (200 to 325 ℃), the predominant oxygen ion is O^- (Reactions (8) and (9)). The adsorbed oxygen takes electrons from the sensing layer, and the thicker depletion layer is formed at the interface, leading to an elevation in electrical resistance. When the target gas is introduced, since all the targets in this study are reducing gases, they react with O^- on the surface (Reactions (10)–(13)), releasing electrons back to the sensing layer [39–41]. This reaction reduces the thickness of the depletion layer, resulting in lower electrical resistance. The sensing procedures can be described as Reactions (8)–(13):

$$O_2(gas) \rightarrow O_2(ads) \tag{8}$$

$$O_2(ads) + 2e^- \rightarrow 2O^- \tag{9}$$

$$CH_3CHCH_3OH + 9O^- \rightarrow 3CO_2 + 4H_2O + 9e^- \tag{10}$$

$$CH_3COCH_3 + 8O^- \rightarrow 3CO_2 + 3H_2O + 8e^- \tag{11}$$

$$HCHO + 2O^- \rightarrow CO_2 + H_2O + 2e^- \tag{12}$$

$$2NH_3 + 5O^- \rightarrow 2NO + 3H_2O + 5e^- \tag{13}$$

In the gas sensing test, the NaZnO1 sensor demonstrated superior responses to all target gases, and its selectivity exhibited significant variations correlating with changes in working temperature. This phenomenon was intricately associated with the adsorption capacity of gas molecules on the sensing material surface and the oxidation–reduction reactions with chemisorbed oxygen [20,42].

On one front, the adsorption capacity of MOS materials for target gases fluctuates with temperature variations, leading to distinct adsorption quantities for the same gas at different temperatures [43,44]. Simultaneously, Na-doped ZnO serves as a catalyst during the oxidation–reduction process. Distinct gases require different activation energies for these reactions (Reactions

Table 1   Comparison of the VOC sensing performance of the Na-doped ZnO sensor and other n-type metal doped ZnO sensors

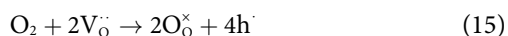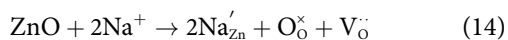| Sensing material	Semiconductor type	Target gas	Concentration (ppm)	T (℃)	S	Response/recovery time	Ref.
K–ZnO	n	Ethanol	100	300	45.2	45 s/17 s	[35]
Na-doped ZnO	n	Ethanol	100	280	37.8	56 s/25 s	[35]
Au/Na-doped ZnO	p	Ethanol	60	RT (UV)	40%	72 s/> 600 s	[36]
Na-doped ZnO	p	Acetone	100	RT (UV)	3.4	18 s/63 s	[20]
Na-doped ZnO	p	NH_3	500	400	1.7	—	[23]
NaZnO1	n	HCHO	5	225	21.3	448 s/836 s	This work
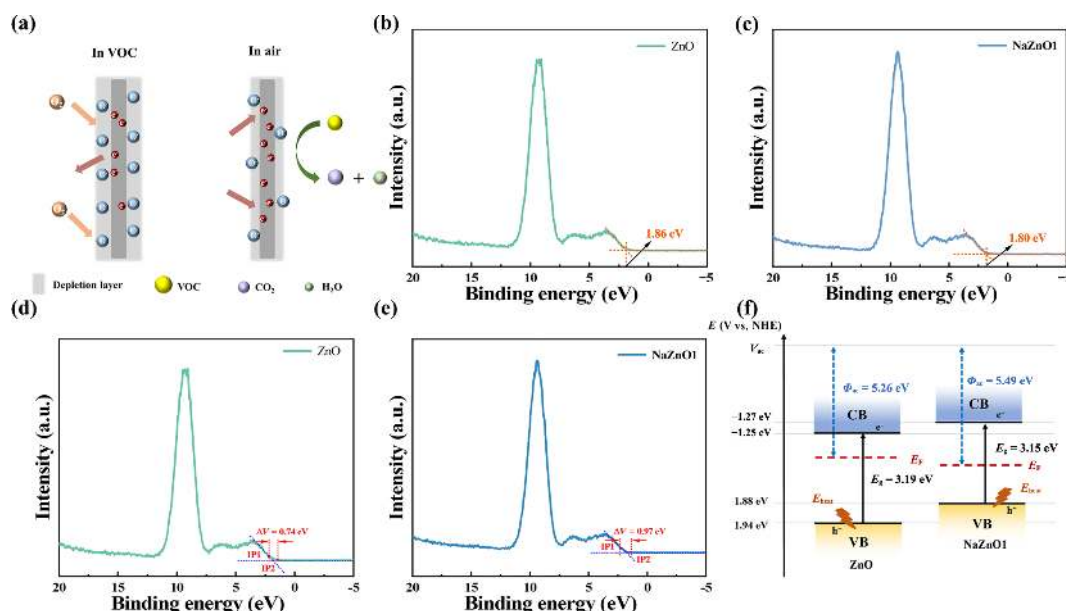
Fig. 8 (a) Gas sensing mechanism for Na-doped ZnO. Work functions of (b) ZnO and (c) NaZnO1. VB-XPS spectra of (d) ZnO and (e) NaZnO1. (f) Band structures of the ZnO and NaZnO1.

(10)–(13)), indicating that the reaction intensity varies at different temperatures [43,45]. This discrepancy results in fluctuations in the number of electron transfers, consequently contributing to differences in sensor responses across temperature variations.

The enhancement of sensing properties can be explained. First, when Na^+ is doped into the lattice of ZnO, the steps can be written as Reactions (14) and (15) [20]:

$$ZnO + 2Na^+ \rightarrow 2Na'_{Zn} + O^{\times}_O + V^{\cdot\cdot}_O \tag{14}$$

$$O_2 + 2V^{\cdot\cdot}_O \rightarrow 2O^{\times}_O + 4h^{\cdot} \tag{15}$$

where Na'_{Zn} represents the Zn^{2+} which were replaced by Na^+, $O^{\times}_O$ is the normal lattice oxygen, and $V^{\cdot\cdot}_O$ is the oxygen vacancy. The holes generated in this step can capture free electrons, which leads to a higher electrical resistance than pure ZnO. According to these equations, when the concentration of Na^+ increased, the concentration of $V^{\cdot\cdot}_O$ increased, which is consistent with the XPS and ICP-OES results. High-concentration oxygen vacancies are beneficial to the sensing performance. Stoichiometric ZnO has a stable lattice structure and low surface activity, which makes it difficult to adsorb oxygen molecules and target VOCs, resulting in weak response and high operating temperature [5,46]. When Na^+ is introduced into the lattice, the substitution of Na^+ and the high concentration of oxygen vacancies disrupt the long-range order of the ZnO crystal structure, resulting in an unsaturated coordination state between impurity ions and oxygen vacancies [32,47,48]. Consequently, the gas sensing layer's surface activity is substantially higher than it is in the undoped state, thereby enhancing the adsorption of gas molecules onto its surface. At the same time, the oxygen vacancies form electron aggregation centers next to the unsaturated Zn atom, which makes it easier for electrons around the metal atom to exchange with adsorbed gas molecules [19]. According to Reactions (8)–(13), the fundamental factor that determines the change in resistance of the gas sensing layer is the exchange of electrons during the adsorption process of oxygen molecules and the target gas. A higher electron exchange rate means that the sensor has a greater change in resistance and better response after VOCs injection. Finally, oxygen vacancies serve as the preferred sites for the adsorption of oxidizing gases,

meaning that more oxygen molecules are preferred to adsorb onto the oxygen vacancy sites formed by doping. Introducing a high concentration of oxygen vacancies leads to a significant increase in the number of adsorbed oxygen ions on the gas-sensing layer's surface. This, in turn, increases the number of reactive VOCs molecules, leading to an enhanced electron exchange between the gas-sensing layer and the gas molecules. Consequently, the sensor's response improves.

To further investigate the role of Na doping on the band structure, the VB-XPS spectra were carried out to obtain the VB potential ($E_{VB,XPS}$) of the ZnO and the NaZnO1 samples. Since the obtained $E_{VB,XPS}$ were based on the vacuum level (Figs. 8(b) and 8(c)), the normal standard hydrogen electrode ($E_{VB,NHE}$) was calculated according to Eq. (16) [38], where φ is the work function of the tester (4.52 eV). Therefore, the $E_{VB,NHE}$ of ZnO and NaZnO1 was 1.94 and 1.88 eV, respectively. Since the bandgaps were calculated according to Fig. 3(b), the conduction band (CB) potential was easy to get. The Φ represents the work function of the MOX materials, which can be calculated by Eq. (17) [38]. ΔV is the contact potential energy which can be obtained according to the adjacent inflection point (IP) of the VB-XPS spectra, as shown in Figs. 8(d) and 8(e). Thus, the working function of ZnO ($\Phi_{ac,ZnO}$) and NaZnO1 ($\Phi_{ac,NaZnO1}$) was 5.26 and 5.49 eV, respectively.

$$E_{VB,NHE} = \varphi + E_{VB,XPS} - 4.44 \text{ eV} \tag{16}$$

$$\Delta V = \Phi - \varphi \tag{17}$$

The final band structure is described in Fig. 8(f). The structure indicated that the Fermi level of Na-doped ZnO was lower than ZnO, which is consistent with the gas-testing results. With the doping of Na^+, the resistances of the Na-doped ZnO sensors were increased due to the decrease of the free electrons.

Additionally, when Na^+ is doped into the ZnO lattice, which is referred to as an impurity, an acceptor level will be introduced into the forbidden gap of ZnO. The acceptor level is near the top of the valence gap [49]. Under the condition of a certain amount of Na^+ doping, the new acceptor level can be in contact with the VB potential, leading to a decrease in the bandgap. Thus, the

narrowed bandgap makes it easier to produce more charge carriers when heated at a lower temperature and significantly improves the sensing performance of the urchin-like Na-doped ZnO sensors.

4 Conclusions

In this work, the Na doping to the ZnO nanoneedles was successfully fabricated by adding Na and citric acid into the precursor for the hydrothermal method. The ICP-OES results demonstrate the significant role of citric acid in realizing Na doping. The Na-doped ZnO sample owned the best gas-sensing performance when the molar ratio of Na : citric acid was 3 : 1 (NaZnO1) for the detection of different kinds of biomarkers for lung cancer. The NaZnO1 sensor exhibited a significantly improved response of 21.3 ppm to 5 ppm HCHO while maintaining good humidity resistance, stability, and excellent selectivity. Furthermore, this performance was achieved at a lower temperature of 225 ℃ and approximately 50% RH. A selectivity change with temperature was observed as well. The NaZnO1 sensor showed excellent selectivity to HCHO at 225 and 200 ℃. Considering the response and recovery time, 225 ℃ was chosen as the optimal working temperature for HCHO detection. The gas sensing mechanism was considered as the oxygen defect and the Na dopant which worked as the acceptor level in the ZnO bandgap. It narrowed the bandgap and provided more free electrons for gas adsorption.

Declaration of competing interest

The authors have no competing interests to declare that are relevant to the content of this article.

Electronic Supplementary Material

Supplementary material is available in the online version of this article at https://doi.org/10.26599/JAC.2024.9220873.

References

[1] Behera B, Joshi R, Anil Vishnu GK, *et al.* Electronic nose: A non-invasive technology for breath analysis of diabetes and lung cancer patients. *J Breath Res* 2019, **13**: 024001.

[2] Sun XH, Shao K, Wang T. Detection of volatile organic compounds (VOCs) from exhaled breath as noninvasive methods for cancer diagnosis. *Anal Bioanal Chem* 2016, **408**: 2759–2780.

[3] Hajivand P, Carolus Jansen J, Pardo E, *et al.* Application of metal–organic frameworks for sensing of VOCs and other volatile biomarkers. *Coord Chem Rev* 2024, **501**: 215558.

[4] Antoniou SX, Gaude E, Ruparel M, *et al.* The potential of breath analysis to improve outcome for patients with lung cancer. *J Breath Res* 2019, **13**: 034002.

[5] Pathak AK, Swargiary K, Kongsawang N, *et al.* Recent advances in sensing materials targeting clinical volatile organic compound (VOC) biomarkers: A review. *Biosensors* 2023, **13**: 114.

[6] Zhang C, Huan YC, Li Y, *et al.* Low concentration isopropanol gas sensing properties of Ag nanoparticles decorated In_2O_3 hollow spheres. *J Adv Ceram* 2022, **11**: 379–391.

[7] Srinivasan P, Prakalya D, Jeyaprakash BG. UV-activated ZnO/CdO n–n isotype heterostructure as breath sensor. *J Alloys Compd* 2020, **819**: 152985.

[8] Yang YZ, Li S, Liu D, *et al.* UV-activated efficient formaldehyde gas sensor based on cauliflower-like graphene-modified In-doped ZnO at room temperature. *J Alloys Compd* 2023, **936**: 168104.

[9] Liu XJ, Duan XP, Zhang C, *et al.* Improvement toluene detection of gas sensors based on flower-like porous indium oxide nanosheets. *J Alloys Compd* 2022, **897**: 163222.

[10] He XX, Chai HF, Luo YF, *et al.* Metal oxide semiconductor gas sensing materials for early lung cancer diagnosis. *J Adv Ceram* 2023, **12**: 207–227.

[11] Zheng ZC, Liu KW, Zhou YW, *et al.* Ultrasensitive room-temperature geranyl acetone detection based on $Fe@WO_{3-x}$ nanoparticles in cooked rice flavor analysis. *J Adv Ceram* 2023, **12**: 1547–1561.

[12] Liu KW, Zhang C. Volatile organic compounds gas sensor based on quartz crystal microbalance for fruit freshness detection: A review. *Food Chem* 2021, **334**: 127615.

[13] Xu JY, Zhang C. Oxygen vacancy engineering on cerium oxide nanowires for room-temperature linalool detection in rice aging. *J Adv Ceram* 2022, **11**: 1559–1570.

[14] Zhao XT, Yang Y, Cheng L, *et al.* Cold sintering process for fabrication of a superhydrophobic ZnO–polytetrafluoroethylene (PTFE) ceramic composite. *J Adv Ceram* 2023, **12**: 1758–1766.

[15] Cheng ZL, Li R, Long YW, *et al.* Power loss transition of stable ZnO varistor ceramics: Role of oxygen adsorption on the stability of interface states at the grain boundary. *J Adv Ceram* 2023, **12**: 972–983.

[16] Postica V, Vahl A, Santos-Carballal D, *et al.* Tuning ZnO sensors reactivity toward volatile organic compounds via Ag doping and nanoparticle functionalization. *ACS Appl Mater Interfaces* 2019, **11**: 31452–31466.

[17] Yuan HY, Aljneibi SAAA, Yuan JR, *et al.* ZnO nanosheets abundant in oxygen vacancies derived from metal–organic frameworks for ppb-level gas sensing. *Adv Mater* 2019, **31**: e1807161.

[18] Qin WB, Yuan ZY, Shen YB, *et al.* Phosphorus-doped porous perovskite $LaFe_{1-x}PxO_{3-\delta}$ nanosheets with rich surface oxygen vacancies for ppb level acetone sensing at low temperature. *Chem Eng J* 2022, **431**: 134280.

[19] Huang GY, Wang CY, Wang JT. First-principles study of diffusion of Li, Na, K and Ag in ZnO. *J Phys: Condens Matter* 2009, **21**: 345802.

[20] Jaisutti R, Lee M, Kim J, *et al.* Ultrasensitive room-temperature operable gas sensors using p-type Na:ZnO nanoflowers for diabetes detection. *ACS Appl Mater Interfaces* 2017, **9**: 8796–8804.

[21] Jasmi KK, Anto Johny T, Siril VS, *et al.* Influence of defect density states on NO_2 gas sensing performance of Na:ZnO thin films. *J Sol Gel Sci Technol* 2023, **107**: 659–670.

[22] Wang CN, Li YL, Gong FL, *et al.* Advances in doped ZnO nanostructures for gas sensor. *Chem Rec* 2020, **20**: 1553–1567.

[23] Mariappan R, Ponnuswamy V, Suresh R, *et al.* Role of substrate temperature on the properties of Na-doped ZnO thin film nanorods and performance of ammonia gas sensors using nebulizer spray pyrolysis technique. *J Alloys Compd* 2014, **582**: 387–391.

[24] Basyooni MA, Shaban M, El Sayed AM. Enhanced gas sensing properties of spin-coated Na-doped ZnO nanostructured films. *Sci Rep* 2017, **7**: 41716.

[25] Meng FL, Qi TY, Zhang JJ, *et al.* MoS_2-templated porous hollow MoO_3 microspheres for highly selective ammonia sensing via a lewis acid–base interaction. *IEEE Trans Ind Electron* 2022, **69**: 960–970.

[26] Li K, Wu YZ, Chen MP, *et al.* High methanol gas-sensing performance of Sm_2O_3/ZnO/$SmFeO_3$ microspheres synthesized via a hydrothermal method. *Nanoscale Res Lett* 2019, **14**: 57.

[27] Sui YR, Song YP, Lv SQ, *et al.* Enhancing of the rapid thermal annealing for the p-type transition in sodium-doped ZnCdO thin films using RF reactive magnetron sputtering synthesis. *J Alloys Compd* 2017, **701**: 689–697.

[28] Zhang DD, Fang Z, Wang L, *et al.* Controllable growth of single-crystalline zinc oxide nanosheets under ambient condition toward ammonia sensing with ultrahigh selectivity and sensitivity. *J Adv Ceram* 2022, **11**: 1187–1195.

[29] Lei ZH, Cheng PF, Wang YL, *et al*. Pt-doped α-Fe₂O₃ mesoporous microspheres with low-temperature ultra-sensitive properties for gas sensors in diabetes detection. *Appl Surf Sci* 2023, **607**: 154558.

[30] Li J, Yang M, Li YY, *et al*. Construction of SnO₂ nanoneural network by ultrasmall particles for highly selective NO₂ detection at low temperature. *Sensor Actuat B-Chem* 2022, **361**: 131703.

[31] Xu HY, Zhang SD, Wang YF, *et al*. New insights into the photocatalytic mechanism of pristine ZnO nanocrystals: From experiments to DFT calculations. *Appl Surf Sci* 2023, **614**: 156225.

[32] Shu Y, Duan XL, Niu Q, *et al*. Mechanochemical alkali-metal-salt-mediated synthesis of ZnO nanocrystals with abundant oxygen vacancies: an efficient support for Pd-based catalyst. *Chem Eng J* 2021, **426**: 131757.

[33] Marzorati D, Mainardi L, Sedda G, *et al*. A review of exhaled breath: A key role in lung cancer diagnosis. *J Breath Res* 2019, **13**: 034001.

[34] Luo YF, Ly A, Lahem D, *et al*. Role of cobalt in Co–ZnO nanoflower gas sensors for the detection of low concentration of VOCs. *Sensor Actuat B-Chem* 2022, **360**: 131674.

[35] Sáaedi A, Yousefi R. Improvement of gas-sensing performance of ZnO nanorods by group-I elements doping. *J Appl Phys* 2017, **122**: 224505.

[36] Hsu CL, Jhang BY, Kao C, *et al*. UV-illumination and Au-nanoparticles enhanced gas sensing of p-type Na-doped ZnO nanowires operating at room temperature. *Sensor Actuat B-Chem* 2018, **274**: 565–574.

[37] Zhang C, Xu KC, Liu KW, *et al*. Metal oxide resistive sensors for carbon dioxide detection. *Coord Chem Rev* 2022, **472**: 214758.

[38] Zhang C, Zheng ZC, Liu KW, *et al*. Highly sensitive and selective Sb₂WO₆ microspheres in detecting VOC biomarkers in cooked rice: Experimental and density functional theory study. *Food Chem* 2023, **424**: 136323.

[39] Luo YF, Ly A, Lahem D, *et al*. A novel low-concentration isopropanol gas sensor based on Fe-doped ZnO nanoneedles and its gas sensing mechanism. *J Mater Sci* 2021, **56**: 3230–3245.

[40] Chai HF, Li Y, Luo YF, *et al*. Investigation on isopropanol sensing properties of LnFeO₃ (Ln = Nd, Dy, Er) perovskite materials synthesized by microwave-assisted hydrothermal method. *Appl Surf Sci* 2022, **601**: 154292.

[41] Zheng ZC, Liu KW, Xu KC, *et al*. Investigation on microstructure and nonanal sensing properties of hierarchical Sb₂WO₆ microspheres. *Ceram Int* 2022, **48**: 30249–30259.

[42] Siril VS, Jasmi KK, AntoJohny T, *et al*. Investigation of thickness effect on NO₂ gas sensing properties of ZnO/Na thin films. *Mater Today Proc* 2023, **76**: 365–371.

[43] Jin XH, Li YW, Zhang B, *et al*. Temperature-dependent dual selectivity of hierarchical porous In₂O₃ nanospheres for sensing ethanol and TEA. *Sensor Actuat B-Chem* 2021, **330**: 129271.

[44] Peng L, Xie TF, Yang M, *et al*. Light induced enhancing gas sensitivity of copper-doped zinc oxide at room temperature. *Sensor Actuat B-Chem* 2008, **131**: 660–664.

[45] Zhang WS, Yuan TW, Wang XH, *et al*. Coal mine gas sensors with dual selectivity at variable temperatures based on a W₁₈O₄₉ ultra-fine nanowires/Pd@Au bimetallic nanoparticles composite. *Sensor Actuat B-Chem* 2022, **354**: 131004.

[46] Zhang C, Geng X, Liao HL, *et al*. Room-temperature nitrogen-dioxide sensors based on ZnO₁₋ₓ coatings deposited by solution precursor plasma spray. *Sensor Actuat B-Chem* 2017, **242**: 102–111.

[47] Yuan H, Xu M, Dong CJ, *et al*. Mechanistic insights into magnetic and gas sensing properties of (F,Na)-codoped ZnO nanocrystals by room-temperature photoluminescence. *Appl Surf Sci* 2019, **496**: 143511.

[48] Sun K, Zhan GH, Zhang L, *et al*. Highly sensitive NO₂ gas sensor based on ZnO nanoarray modulated by oxygen vacancy with Ce doping. *Sensor Actuat B-Chem* 2023, **379**: 133294.

[49] Zhang C, Geng X, Li JW, *et al*. Role of oxygen vacancy in tuning of optical, electrical and NO₂ sensing properties of ZnO₁₋ₓ coatings at room temperature. *Sensor Actuat B-Chem* 2017, **248**: 886–893.